ELSEVIER

Contents lists available at ScienceDirect

### Materials Science & Engineering A

journal homepage: www.elsevier.com/locate/msea





## Fabrication of spatially-variable heterostructured CoCrFeMnNi high entropy alloy by laser processing

Jiajia Shen <sup>a,b,\*\*</sup>, Yeon Taek Choi <sup>c</sup>, Jin Yang <sup>d</sup>, Jingjing He <sup>e</sup>, Zhi Zeng <sup>f</sup>, N. Zhou <sup>g</sup>, A.C. Baptista <sup>b</sup>, Hyoung Seop Kim <sup>c,h,i</sup>, J.P. Oliveira <sup>a,b,\*</sup>

- <sup>a</sup> UNIDEMI, Department of Mechanical and Industrial Engineering, NOVA School of Science and Technology, Universidade NOVA de Lisboa, 2829-516, Caparica, Portugal
- b CENIMAT/13N, Department of Materials Science, NOVA School of Science and Technology, Universidade NOVA de Lisboa, 2829-516, Caparica, Portugal
- <sup>c</sup> Department of Materials Science and Engineering, POSTECH (Pohang University of Science and Technology), Pohang, 37673, South Korea
- d School of Materials Engineering, Shanghai University of Engineering Science, Shanghai, 201620, China
- <sup>e</sup> Advanced Manufacturing Center, Ningbo Institute of Technology, Beihang University, Ningbo, 315800, China
- f School of Mechanical and Electrical Engineering, University of Electronic Science and Technology of China, Sichuan, 611731, China
- g Department of Mechanical and Mechatronics Engineering, University of Waterloo, 200 University Avenue West, Waterloo, ON, N2L 3G1, Canada
- h Graduate Institute of Ferrous Technology, POSTECH (Pohang University of Science and Technology), Pohang, 37673, South Korea
- <sup>1</sup> Institute for Convergence Research and Education in Advanced Technology, Yonsei University, Seoul, 03722, South Korea

#### ARTICLE INFO

# Keywords: CoCrFeMnNi high entropy alloy Heterostructures Pulsed laser processing Mechanical properties testing

#### ABSTRACT

This study investigates the fabrication of spatially-variable heterostructured CoCrFeMnNi high entropy alloy (HEA) using pulsed laser processing. Two distinct fabrication approaches, involving single-(SP) and double-sided (DP) laser passes, were employed. Microstructural characterization through electron backscatter diffraction revealed significant differences. SP-HEA exhibited a spatially heterogeneous microstructure with coarse columnar grains, while DP-HEA displayed a sandwich-like structure with fine equiaxed recrystallized grains. Microhardness mapping demonstrated a gradient trend in SP-HEA, with the fusion zone exhibiting the lowest hardness and the base material the highest. In contrast, DP-HEA displayed an overall soft-hard-soft structure. Tensile testing revealed distinct mechanical responses, with DP-HEA exhibiting higher strength and ductility compared to SP-HEA. The improved performance of DP-HEA was attributed to a more uniform distribution of heterogeneity, minimizing mechanical interactions between soft and hard domains. Moreover, corrosion resistance was assessed, showing that DP-HEA outperformed SP-HEA and non-processed material, suggesting superior stability in corrosive environments. These findings highlight the profound influence of fabrication parameters on the microstructure and mechanical properties of spatially-variable heterostructured HEAs. The study contributes valuable insights for material design and applications based on CoCrFeMnNi high entropy alloys.

#### 1. Introduction

In recent years, high entropy alloys (HEAs) have attracted extensive research attention due to their excellent structural stability and promising mechanical properties [1–5]. Among the various HEAs, the equiatomic CoCrFeMnNi HEA, known as the Cantor alloy, has been widely investigated for its outstanding mechanical performance over wide temperature ranges. However, despite its favorable mechanical

properties, the CoCrFeMnNi HEA still exhibits relatively low yield strength at room temperature [6–8]. To achieve broader applications prospects, it is imperative to overcome the inherent trade-off between strength and plasticity typically observed in materials with homogeneous microstructures. Therefore, the development of a synergistic structure that reconciles both high strength and ductility becomes crucial

Since the first report in 2017 on heterostructured metallic materials

E-mail addresses: j.shen@campus.fct.unl.pt (J. Shen), jp.oliveira@fct.unl.pt (J.P. Oliveira).

<sup>\*</sup> Corresponding author. CENIMAT/I3N, Department of Materials Science, NOVA School of Science and Technology, Universidade NOVA de Lisboa, 2829-516, Caparica, Portugal

<sup>\*\*</sup> Corresponding author. CENIMAT/I3N, Department of Materials Science, NOVA School of Science and Technology, Universidade NOVA de Lisboa, 2829-516, Caparica, Portugal.

[9], with superior mechanical properties that cannot be explained by traditional materials science approaches, researchers have focus on microstructural design. These materials are typically processed into various microstructural configurations, including gradient structures [10–13], heterogeneous layer structures [14], bimodal structures [15–17], and harmonic structures [9,18–20]. They all share a common feature: the combination of soft and hard domains [21,22], resulting in an exciting harmony of strength and ductility. Numerous studies [23–25] have shown that this exceptional mechanical performance arises due to heterogeneous deformation induced (HDI) strengthening and HDI strain hardening. HDI strengthening is employed to enhance yield strength, while HDI strain hardening helps maintaining ductility.

Currently, most methods for designing heterostructures primarily focus on surface modification techniques [26–28] or heat treatments [29–31]. In comparison to traditional heterogeneous structures, spatially heterogeneous structures offer the potential for more precise functional design and performance optimization. However, research on the design of gradient microstructures with spatial heterogeneity is relatively limited. Particularly, for CoCrFeMnNi HEA, there have been only six studies on improving their mechanical properties using spatially heterogeneous structures, primarily focusing on laser metal deposition [32,33] and laser powder bed fusion [34–36] techniques.

To further expand the engineering applications of CoCrFeMnNi HEAs, pulse laser processing is introduced to create heterogeneous microstructures in this work. Starting with a severely cold rolled base material (BM), a laser source is used to locally melt and promote solid-state transformation targeting the development of a microstructure gradient along the material thickness. Two different spatial heterogeneous structure design strategies were developed: single- and double-side multi-pass processing on the material surface. Obvious differences in microstructure and mechanical performance are rationalized based on electron backscatter diffraction (EBSD), microhardness and tensile testing. A correlation between thermal cycle, microstructure evolution and resulting properties is detailed, providing new insights for the design of spatial heterogeneous structures based on HEAs.

#### 2. Experimental procedure

An equiatomic composition of the CoCrFeMnNi high entropy alloy (HEA) was used in this study. The alloy underwent cold rolling at room

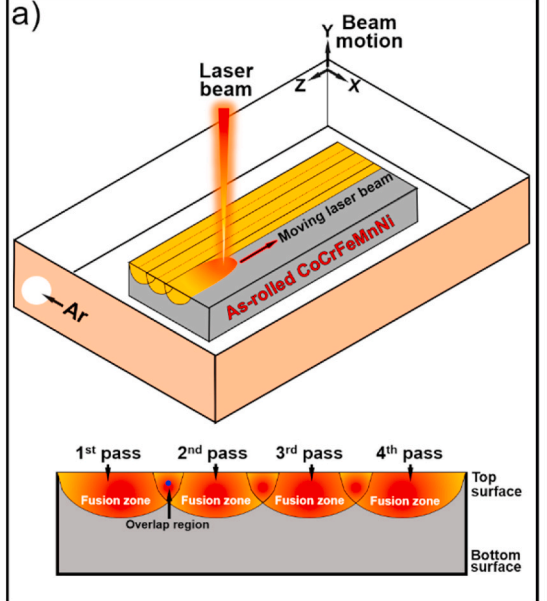
temperature with a 50% thickness reduction, resulting in a final material thickness of 1.5~mm.

To fabricate a spatially distributed heterogeneous microstructure, pulsed laser processing was employed on the CoCrFeMnNi BM. Two distinct approaches were selected. The first involved the use of multipass laser pulses exclusively on the upper surface of the BM along with the resulting cross-sectional in the bottom-side, as depicted in Fig. 1 a). This material condition will be referred to as SP-HEA. The second approach entailed the use of multiple laser passes on both the upper and bottom surfaces of the rolled HEA, as shown in Fig. 1 b). The bottom-side of Fig. 1 b) is the schematic of the experimental setup representing the cross-section for this process, with the material being designated as DP-HFA

Laser processing was conducted with a Nd: YAG laser (wavelength of 1064 nm). The processing parameters were kept constant and included a peak pulse power of 1.15 kW, a duration of 10 ms, a beam spot size of 650  $\mu m$ , and a Gaussian distribution of the laser beam with a 25% overlap between consecutive laser pulses. Argon (Ar) was used as the shielding gas.

After welding, electrical discharge machining (EDM) was used to obtain dog-bone shaped samples (gauge length and width:  $26.11 \times 1.5$ mm) for microstructure and mechanical characterization. For microstructure characterization, EBSD analysis was conducted to evaluate the local microstructure changes induced by the laser processing (detailed information about EBSD experiments can be found in the supplementary materials section). For mechanical characterization, microhardness testing and tensile testing were performed. Microhardness mapping was performed using a Vickers hardness tester (ZwickRoell Indentec). The idents were made by applying a load of 200 g and a dwell time of 10s, with each indentation spaced by 150  $\times$  150  $\mu m$  in both horizontal and vertical directions, enabling to fully probe the different regions across the joint. For the mechanical tensile testing, a strain gauge extensometer from Shimadzu, with a gauge length of 30 mm was used. Room temperature tensile testing, and the tensile test was performed perpendicular to the laser travel direction, with three repeats, was conducted at a strain rate of  $1 \times 10^{-3} \text{s}^{-1}$ . The fracture surfaces were analyzed using scanning electron microscopy (SEM).

Aside from analyzing the microstructure and mechanical properties of the processed materials, other functional properties can be evaluated. In this case, the corrosion resistance of these material is also important



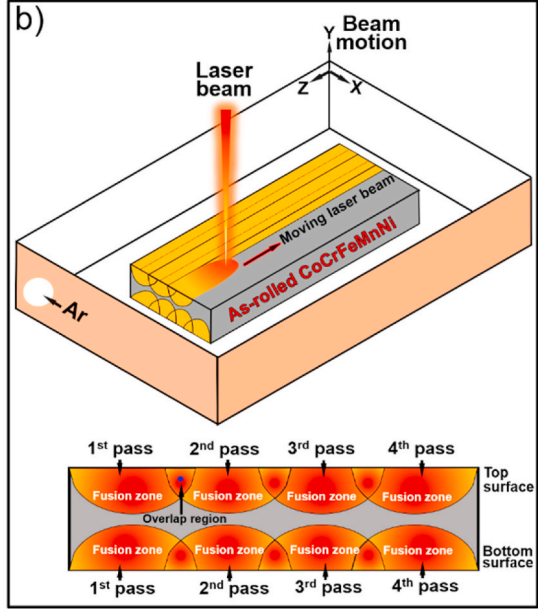


Fig. 1. a) and b): Top-side schematic is the experimental setup of the pulsed laser processing used for fabricated SP-HEA and DP-HEA, respectively, the bottom-side schematic is their cross-sectional.

to be understood given their potential industrial applications. In the current work, Electrochemical characterisation was performed in a conventional three-electrode setup using a potentiostat/galvanostat Interface 1010 from Gamry Instruments. The sample was connected to the working electrode, a platinum wire was used as the counter electrode and an Ag/AgCl electrode was used as the reference electrode. The samples were immersed in a 3.5% wt. NaCl electrolyte solution for 1 h to establish a steady state of the open circuit potential (OCP). Potentiodynamic polarization measurements were immediately conducted at a scan rate of 1 mV/s in the voltage range from -1.5 to 1.5 V. Electrochemical impedance spectroscopy (EIS) measurements were subsequently performed on these samples across a frequency range from 1 Hz to 100 kHz.

#### 3. Results and discussion

Fig. 2 details the microstructural features of SP-HEA. Due to the utilization of multiple laser passes with the same parameters, multiple neighboring fusion zones (FZ) will exist. Within Fig. 2, the white dashed line represents the interface between the FZ and the heat affected zone (HAZ), while the white dotted line indicates the interface between the HAZ and the original as-rolled BM.

According to Fig. 2 a), SP-HEA exhibits an obvious spatial heterogeneity in its microstructure. Moving from the upper (processed) surface to the bottom of the sample (refer to Fig. 2 b, c, and d), the microstructure of SP-HEA evolves as follows: i) coarse columnar grains in the FZ; ii) significantly coarse grains, compared to the BM, in the HAZ adjacent to the FZ; recovered and recrystallized grains in the HAZ near the BM; iv) highly deformed pancake-like grains in the BM.

The formation and evolution of the unique spatially-distributed heterogeneous microstructure is primarily mainly driven by the process heat input, but also by the previous thermomechanical processing of the BM, which possessed a large amount of previously stored strain energy due to cold rolling. Specifically, the highly concentrated laser heat source acts directly on the upper surface of the material, which

subsequently undergoes melting and allows the development of a highly orientated solidification microstructure, promoting the growth of coarse columnar grains (approximately ≈27.17 µm, refer to Fig. 2 e)) which grow perpendicularly to the FZ boundaries. However, no major preferential grain orientation is observed in the FZ (Fig. 2 c)). The heat input used for partial melting will be transferred by conduction along the material thickness increasing its temperature and promoting the development of solid-state transformations in the HAZ. In this region, and closer to the FZ boundary, where the temperature is higher, grain growth is preferential. Here, the grains grew from less than  $<1~\mu\text{m}$ , in the BM, to  $\approx$ 4.22  $\mu m$  (refer to Fig. 2 f)). Furthermore, a large number of fine equiaxed grains (approximately  $\approx 1.54~\mu m,$  refer to Fig. 2 f)) were observed in the HAZ near the BM, where the peak temperature was lower, which is a typical feature of recrystallization phenomena. Thus, the microstructure changes that occurred in the HAZ (refer to Fig. 2 c)) are dependent on the temperature-dependent profile experienced along the material thickness. The bottom layer of the spatial heterogeneous microstructure comprised the as-rolled BM, which is unaffected by the process thermal cycle. Due to its previous deformation, this region exhibits a thin pancake-like morphology. Interestingly, this spatially heterogeneous structure also exhibits a certain level of spatial nonuniformity in grain size (refer to Fig. 2 f)). In particular, the grain size from the top, middle, and bottom regions changes from  $\approx$ 27.17  $\mu$ m,  $\approx$ 4.22 µm, and less than 1 µm, respectively). It should be mentioned that the processing conditions were selected so that full penetration was not achieved. This would allow for the processed material to present different microstructure features, with correspondingly different mechanical responses. Here, it is worth mention that for SP-HEA, the process parameters were deliberately chosen to prevent full penetration of the material. This intentional selection aimed to control the heat input and ensure a specific weld thermal cycle, contributing to the unique microstructural features observed in the current study.

To qualitatively evaluate the strain distribution of the processed material, Fig. 2 b) presents the Kernel Average Misorientation (KAM) maps, while Fig. 2 e) provides the average KAM values for different

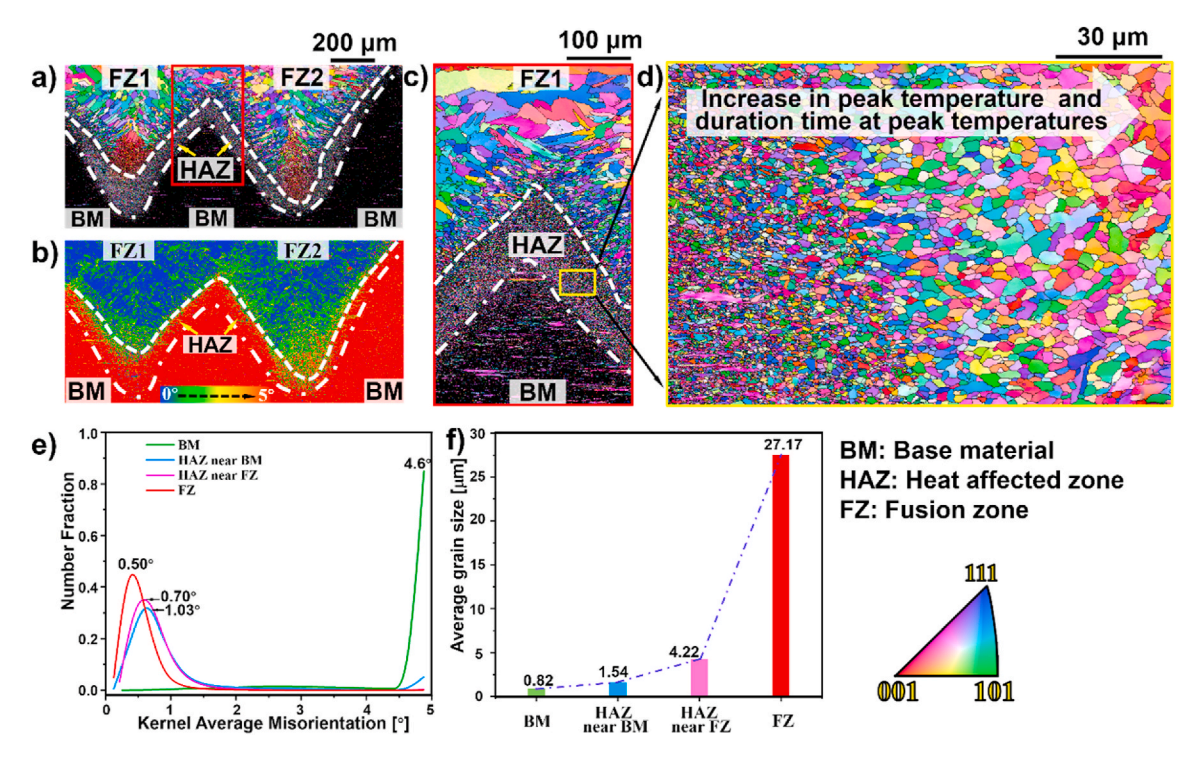


Fig. 2. a) and b): IPF and KAM maps of two adjacent FZ; c): IPF maps of the inserted red box in Fig. 2 a); d): IPF maps of inserted yellow box in Fig. 2 c); e) and f): variation of KAM and grain size with respect to the different regions of the heterostructures, respectively. (For interpretation of the references to colour in this figure legend, the reader is referred to the Web version of this article.)

regions. Here, it should be mentioned that the magnitude of KAM values is typically associated with dislocation density and local plastic deformation, where higher KAM values indicate higher levels of plastic strain. By combining the information from Fig. 2 b) and 2 e), it can be observed that the KAM values increase progressively from the upper surface to the bottom surface of the spatially heterogeneous structure in the following order: KAM<sub>FZ</sub> < KAM<sub>HAZ near the FZ</sub> < KAM<sub>HAZ near the BM</sub> < KAM<sub>BM</sub>. Initially, the high dislocation density contained in the BM is a result of the significant plastic deformation it experienced during cold rolling. Moving away from the BM toward the top surface, the dislocation density decreases, reaching its lowest value in the FZ. This is because the process thermal cycle consumes the pre-existing dislocations via recovery and recrystallization phenomena, in the HAZ, and melting of the FZ completely erased any trace of the material previous thermomechanical processing, making this region resemble that of an as-cast material.

Fig. 3 presents the microstructure of DP-HEA material, where laser pulses were applied on both surfaces of the previously cold rolled material. Again, multiple adjacent FZ exist, but now the area of the non-affected BM is virtually absent now (refer to Fig. 3 a)). In Fig. 3, the white dashed line indicates the HAZ/FZ interface.

Compared to the spatially heterogeneous structure exhibited by SP-HEA, DP-HEA shows a more sandwich-like structure (refer to Fig. 3 a) and 3 c)). Specifically, at mid thickness the HAZ consists of fine equiaxed recrystallized grains, while the upper and bottom parts are primarily composed of coarse dendritic grains in the FZ.

To further visualize and analyze the microstructural features of the spatially heterogeneous structure in DP-HEA, the inverse pole figure (IPF) and  $\Sigma$ 3 twin boundaries within the black dashed box of Fig. 3 a) are given in Fig. 3 c) and d), respectively. From the IPF in Fig. 3 c), it is evident that this spatially heterogeneous structure can be divided into an FZ with coarse dendritic grains and a HAZ which experienced sufficient driving force for recrystallization. In fact, the formation of this spatially heterogeneous structure is primarily attributed to the more complex thermal cycle experienced by the material: each pulse that impinged the material will transfer energy in depth, and near the surfaces a melt pool will be formed. However, near the mid thickness of the CoCrFeMnNi HEA, the previously highly cold rolled material is subjected to a two-step (one per each surface pulse) short heat treatment that is enough to drive recovery and recrystallization phenomena after the FZ boundaries. Consequently, the grain size in the upper and bottom FZ is approximately  $\approx 12.66 \, \mu m$  and  $\approx 18.43 \, \mu m$ , respectively, while the recrystallized grains in the middle HAZ exhibit an equiaxed morphology with a size of approximately  $\approx 3.15 \, \mu m$ . It is worth mentioning that this design concept of this spatially heterogeneous structure now aimed to eliminate the microstructure features that originally existed in the asrolled BM. The presence of a significant number of annealing twins is detected in the HAZ near the FZ, indicating that the process thermal cycles can form these  $\Sigma 3$  twins in the previously cold-rolled material (highlighted by red solid lines in Fig. 3 d). Interestingly, compared to the highly uneven strain gradients observed in the spatially heterogeneous structure of SP-HEA, the strain distribution in the spatially heterogeneous structure of DP-HEA is minimal (KAM $_{TOP}$   $_{FZ} \approx 0.52^\circ$ , KAM $_{HAZ} \approx 0.72^\circ$ , KAM $_{Bottom}$   $_{FZ} \approx 0.52^\circ$ ), approaching overall homogeneity (refer to Fig. 3 b) and 3 e)).

By analyzing the EBSD results of the two different spatially heterogeneous structures (SP-HEA and DP-HEA) described above, it can be inferred that the interactions between the different domains (soft and hard zones) within these heterostructures will inevitably lead to different degrees of mechanical response under the action of external forces. This will be discussed next.

To further investigate the differences in strength between the two prepared spatially heterogeneous structures, microhardness maps for SP-HEA and DP-HEA are given in Fig. 4 a) and b), respectively. In order to facilitate a direct comparison of the hardness magnitudes between both spatially heterogeneous structures, their hardness ranges were set

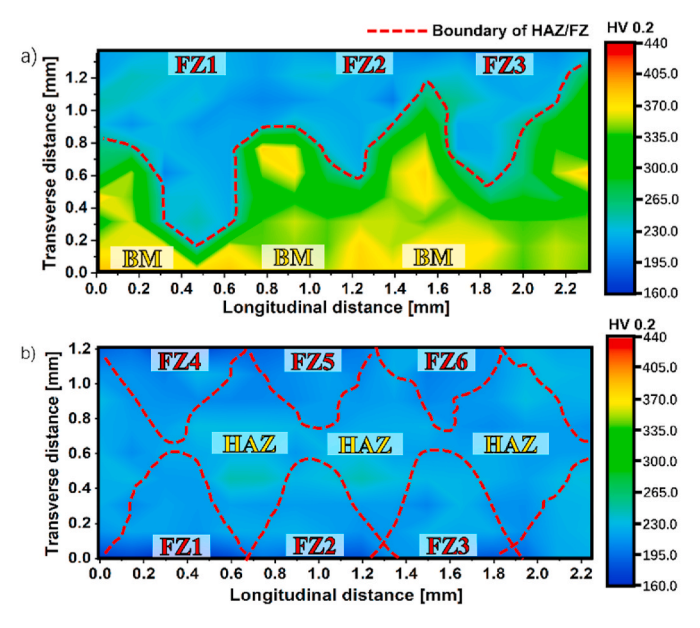


Fig. 4. a) and b) Microhardness maps of SP-HEA and DP-HEA, both in the range of 160-440 HV0.2.

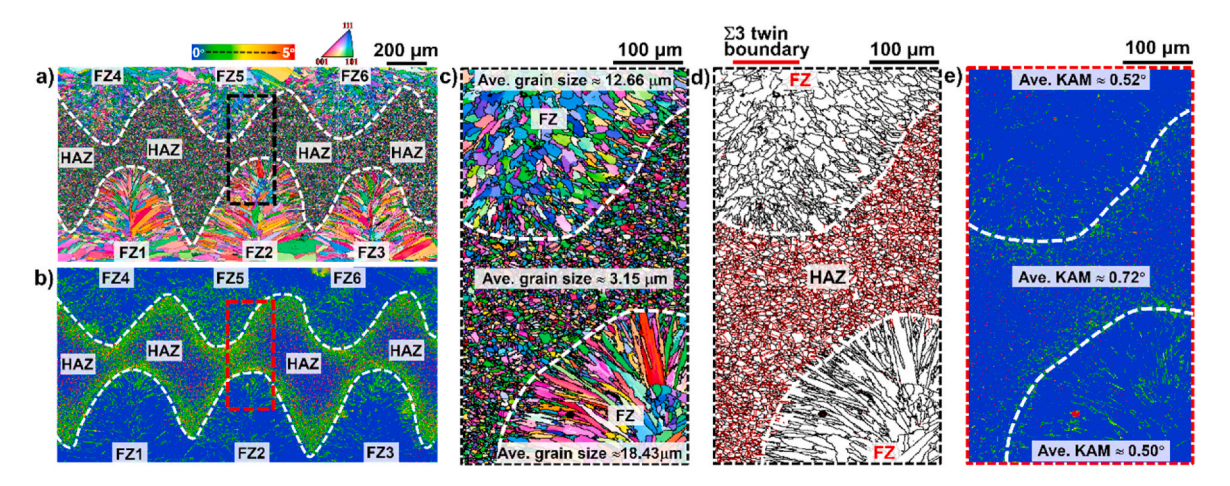


Fig. 3. a) and b): IPF and KAM maps of three adjacent FZ; b),c) and d): IPF,  $\Sigma 3$  twin boundaries map and KAM maps of the dashed rectangular box inserted in Fig. 3 a).

within the same interval, both in the range of 160-440 HV0.2.

For SP-HEA (refer to Fig. 4 a)), a hardness gradient can be clearly observed, with a soft-hard-super hard trend in the spatial distribution from the top to the bottom surface. As expected, the FZ, characterized by coarse dendrites (refer to Fig. 2 a)), exhibits the lowest hardness, approximately  $\approx$  188 HV0.2. Upon entering the HAZ, corresponding to the green region in Fig. 4 a), hardness increases to around  $\approx$ 230 HV0.2. This increase can be attributed to the thermal cycle induced by laser processing, which mimics the effects of high-temperature and lowtemperature annealing (depending on the distance to the heat source) on the previously rolled material. As a result, the stored strain energy in the BM is released, promoting solid-state phase transformations such as recovery, recrystallization, and grain growth to occur. The highest hardness, about ≈440 HV0.2, is found at the bottom of the heterogeneous spatial structure, i.e., in the rolled BM region, which is not affected by the laser processing. The HAZ formed corresponds to a transition domain in terms of material hardness.

Now attention turns to the hardness distribution of DP-HEA (refer to Fig. 4 b)). This heterogeneous structure shows an overall soft-hard-soft sandwich-like structure. However, it should be mentioned that in DP-HEA, the hardness variability between the soft and hard domains is lower than in SP-HEA ( $\approx\!100~\text{vs}\approx250~\text{HV}0.2$ ), which is mainly attributed to the disappearance of the cold rolled microstructure due to the multiple laser pulses impinging both material surfaces. Specifically, the FZ in the upper and bottom parts has an average hardness of approximately  $\approx\!210~\text{HV}0.2$ , while in the HAZ there is a less pronounced increase in hardness to around  $\approx\!235~\text{HV}0.2$ . In addition, the highest hardness value in the entire SP-HEA occurs in the HAZ between two FZs and is about  $\approx\!260~\text{HV}0.2$ , and the lowest harness values were found in the FZ near the upper and bottom surface of the material, at about  $\approx\!160~\text{HV}0.2$ .

Indeed, for the above two spatially heterogeneous structures (SP-HEA and DP-HEA), their hardness distribution is consistent with the

Hall-Petch effect and the classical Taylor hardening model [37], i.e., the strength (hardness) of the metallic material increases monotonically with decreasing grain size (refer to Figs. 2 f) and Fig. 3 c)) and increasing dislocation density (refer to Figs. 2 d) and Fig. 3 e)). Here, it is important to emphasize that although the difference in hardness between the soft and hard domains can enhance HDI strengthening, it cannot be solely relied upon to predict HDI strengthening effects and associated material performance. This is because, in heterogeneous structures, the difference in hardness does lead to the accumulation of dislocations in the soft domain, resulting in higher back stresses, which contributes to enhanced HDI strengthening. However, it is crucial to note that back stresses primarily play a dominant role in HDI strengthening and typically occur during the elastic deformation stage of the material. Once the material enters the plastic deformation stage, HDI strengthening is the result of the synergistic interaction between back stresses in the soft domain and forward stresses in the hard domain.

To further evaluate the applicability of SP-HEA and DP-HEA heterogeneous structures in structural applications, Fig. 5 a) presents the tensile stress-strain curves for these two heterogeneous structures. The black and red lines correspond to SP-HEA and DP-HEA, respectively. As expected, the different heterogeneous microstructures lead to variations in mechanical properties, and both conditions exhibit different mechanical responses. Although both show a reduction in strength compared to the existing homogenously rolled CoCrFeMnNi HEA [37], there is a significant improvement in ductility.

Interestingly, DP-HEA exhibits higher maximum strength ( $\approx$ 570 vs.  $\approx$  693 MPa) and ductility ( $\approx$ 11.0 vs.  $\approx$  18.9 %) compared to SP-HEA (refer to Fig. 5 a)). This difference can be mainly attributed to the distinct spatial heterogeneity in the resulting microstructures, leading to different interactions between the soft and hard domains. Typically, in heterogeneous structures, both the soft and hard domains undergo elastic deformation first when subjected to external loading, similar to conventional homogeneous materials. However, as the loading

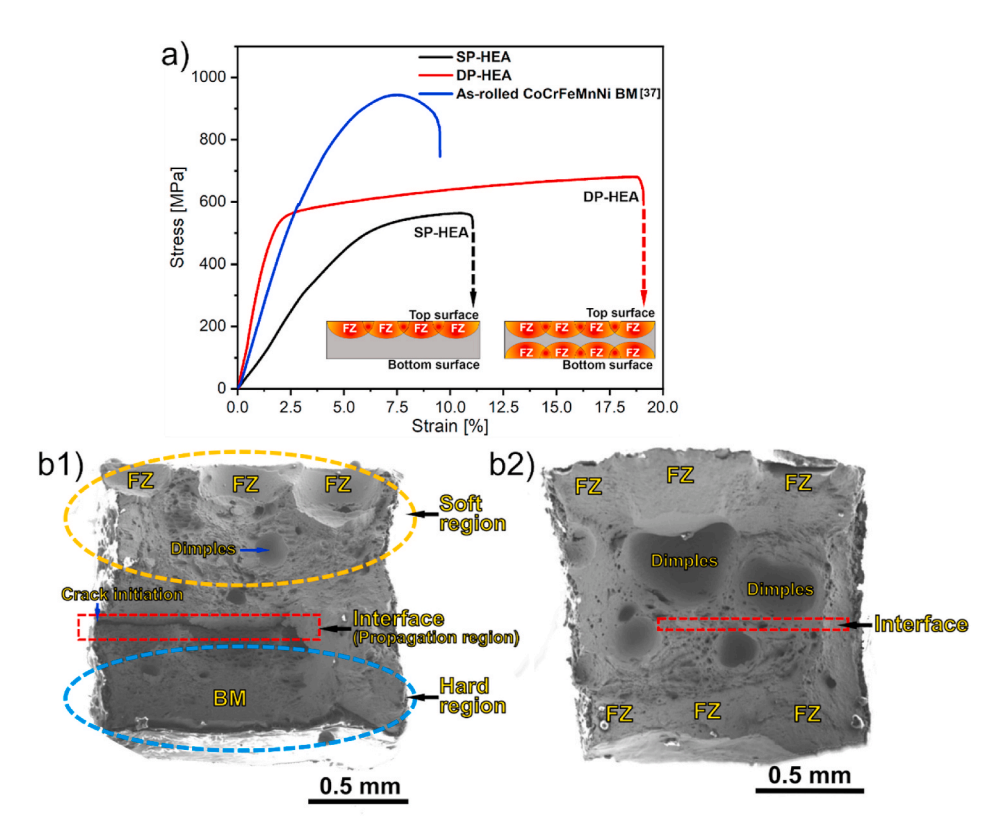


**Fig. 5.** a): Tensile stress-strain curves of SP-HEA (black line), DP-HEA (red line) and as-rolled CoCrFeMnNi BM [37] at room temperature under a strain rate  $10^{-3}$  s<sup>-1</sup>; b1) and b2): Fracture surface analysis of the SP-HEA and DP-HEA. (For interpretation of the references to colour in this figure legend, the reader is referred to the Web version of this article.)

increases, the soft domain will preferentially initiate plastic deformation while the hard domain not, leading to the existence of a mechanical incompatibility. This results in the generation of geometrically necessary dislocations (GNDs) near the interface between the soft and hard domains, which accumulate at the interface and induce heterodeformation induced (HDI) strengthening [38-40]. Theoretically, heterogeneous materials are characterized by significant strength differences between soft and hard domains. The larger the strength differences between domains, the higher mechanical incompatibility, and higher back stresses accumulate in the soft domains, leading to enhanced HDI strengthening and strain hardening. So far, numerous researchers have successfully utilized these strengthening concepts to fabricate spatially heterogeneous structural materials with excellent mechanical properties [41-46]. However, the final mechanical properties of the fabricated spatially heterogeneous materials can be affected by a variety of factors, such as alloy composition, purity of the original materials, synthesis methods, and subsequent processing techniques employed in the fabricated spatially heterogeneous structures. Thus, direct one-to-one property comparisons between the present pulsed laser-processed spatial heterogeneous materials (SP-HEA and DP-HEA) and other spatial heterogeneous materials produced using alternative fabrication methods would lead to biased comparisons. Therefore, in this case, the comparison with spatially heterogeneous materials made by other processes is not performed. Instead, a comparative analysis was performed, focusing on the same original as-rolled CoCrFeMnNi used as a benchmark for mechanical properties [37]. The present results demonstrate that SP-HEA and DP-HEA exhibit superior performance in terms of ductility (18.9% vs. 11.0% vs. 9.5%, for SP-HEA, DP-HEA, and as-rolled CoCrFeMnNi, respectively), albeit with reduced strength when compared to the as-rolled CoCrFeMnNi (693 MPa vs. 570 MPa vs. 947 MPa), showcasing the potential application of these two heterostructured materials (SP-HEA and DP-HEA) for structural applications where depending on the expected loading conditions, one can chose either processing methodology. An intriguing observation arises from the tensile stress-strain curves, specifically in the elastic deformation stage, where the slope of SP-HEA is discernibly lower than that of DP-HEA. This discrepancy suggests that, under equivalent external loading, SP-HEA undergoes a more substantial deformation. To elucidate this behavior, delving into the dynamics of loading transfer and the dimensions of the load-bearing area for both SP-HEA and DP-HEA is necessary. In materials featuring both soft and hard regions, the initial load during external loading is borne by the softer regions due to their inherent characteristics. As these soft regions yield, the load gradually transfers to the harder regions. Additionally, considering the load-bearing area, a larger object subjected to the same external load experiences relatively lower force per unit area. Therefore, to achieve an equivalent deformation, the load applied to the larger load-bearing area must surpass that applied to the smaller force-bearing area. Applying these principles to SP-HEA and DP-HEA, the stress-strain curve reveals a lower elastic slope for SP-HEA, indicating higher deformation under the same external load. This can be primarily attributed to the fact that the area of relatively soft regions in DP-HEA is nearly twice that of SP-HEA. When subjected to the same external load, the initially stressed areas—represented by the FZ—exhibit varying force per unit areas due to the doubled FZ area in DP-HEA. Consequently, the external load required to induce yielding in the soft region of DP-HEA is significantly greater than that in SP-HEA, thereby contributing to the observed difference in elastic slopes. Returning to the current work, the strength (hardness) difference between the soft and hard domains in SP-HEA is significantly larger than in DP-HEA, 100 vs 252 HV0.2, respectively. Therefore, the mechanical performance of SP-HEA would be expected to be better than that of DP-HEA. However, DP-HEA demonstrates superior mechanical properties in terms of both strength and plasticity than SP-HEA. An initial inference is that the large strength difference ( $\approx$ 210 vs.  $\approx$ 400 HV0.2) between the soft domain (FZ) and the hard domains (rolled BM) in SP-HEA results in massive mechanical incompatibility at the

interface. The highly concentrated strain gradient leads to a large accumulation of dislocations at the interface, inducing stress concentration and crack initiation, ultimately resulting in failure at the soft-hard interface. This inference is supported by the observed fracture locations of SP-HEA, as indicated in Fig. 5 b1). On the contrary, the improved mechanical performance of DP-HEA can be attributed to its relatively uniform distribution of heterogeneity at the microstructure level, with a small strength difference between the hard and the soft domains ( $\approx$ 230 vs  $\approx$  210 HV0.2). This minimizes the mechanical interactions between them and reduces the potential for stress concentrations. Additionally, this more homogeneous microstructure distribution allows for better stress absorption and dispersion, enhancing the material's toughness and ductility. These factors collectively contribute to the improved mechanical properties of DP-HEA, which is further corroborated by the observed ductile fracture mode with numerous dimples on the fracture surface of Fig. 5 b2). Here, a special explanation is needed for the states of stress concentration in heterostructured materials. It is known that during the plastic deformation of heterostructured materials, the hetero zones deform in-homogeneously, generating back stresses in the soft zones and forward stresses in the hard zones. Back stress originates from the accumulation of dislocations in the soft zone, which will act to impede dislocation slip in the soft zone promoting a strain-hardening effect. Forward stresses are created in the hard zone due to stress concentrations at the zone boundary caused by dislocation pileup. For heterostructured materials, HDI strengthening is typically the result of the synergistic effect of both back and forward stresses: the back stresses act to enhance the HDI strengthening, while the forward stresses act to limit the HDI strengthening by assisting the plastic deformation in the hard zones. Therefore, compared to DP-HEA, where the difference between the soft and hard gradients is relatively small ( $\approx$ 100 vs  $\approx$  252 HV0.2), the high dislocation density generated in the soft zone of SP-HEA (refer to Fig. 2 b)) causes a high stress concentration that occurs at the soft/hard interface, which inevitably generates high forward stresses in the hard domain. As a result, the higher forward stresses in SP-HEA weaken the HDI strengthening in a more abrupt way in DP-HEA. Therefore, a significant difference in hardness between the soft and hard domains can lead to high stress concentrations at the interface, increasing the risk of crack initiation and eventually fracture. Additionally, excessive stress concentration can induce high forward stresses within the hard domain, which in turn weakens the HDI strengthening effect. Thereby, the magnitude of hardness difference is just one factor affecting HDI strengthening, and the actual material performance is determined by the interaction of multiple factors. Thus, the exceptional mechanical properties observed in DP-HEA can be attributed to the combined effects of multiple factors. While the introduction of back stresses theoretically suggests the possibility of stress concentration, DP-HEA exhibits a more balanced microstructural distribution, leading to improved stress absorption and dispersion. Additionally, the smaller strength disparities between the soft and hard domains contribute to reduced mechanical incompatibility. In DP-HEA, there exists a relatively moderate hardness difference between the soft and hard domains, effectively reducing the back stress from the hard zone. Furthermore, the processing conditions, involving an optimized microstructure, play a crucial role in alleviating this stress concentration effect. These conditions further enhance the material's strength and ductility. This complex interplay of factors highlights the intricate relationship between microstructure and mechanical performance in heterogeneous materials. In addition, through a comparative analysis of two spatially heterogeneous materials (SP-HEA and DP-HEA) prepared using different laser processing techniques, it has been confirmed that the applicability of the back stresses strengthening effect (HDI strengthening) depends on the specific characteristics of the material and the associated processing conditions. Here, it is worth mention that, the current work was focus on comparing and analyzing the microstructural characteristics and mechanical properties between the two distinct spatially heterogeneous structures (SP-HEA and

DP-HEA). However, future endeavors will primarily concentrate on systematically investigating a broader range of laser parameters to fabricate spatially-variable heterostructured CoCrFeMnNi high entropy alloy through laser processing. This expanded exploration aims to gain a more comprehensive understanding of how different laser parameters impact the microstructure and mechanical properties of CoCrFeMnNi high entropy alloy.

To assess the corrosion behavior of the processed materials, Fig. 6 presents the anodic polarization curves of the BM, SP-HEA, and DP-HEA. Overall, all three exhibit favorable passivation characteristics. However, upon closer inspection in the enlarged view in Fig. 6, it is evident that the passivation potential range of the BM is broader, with that of the SP-HEA condition being slightly lower. This implies that the passivation film formed on BM has a more stable corrosion resistance, followed by that of the DP-HEA processed material. Additionally, noteworthy is the breakdown voltage (indicated by solid yellow circles), representing the potential corresponding to the initiation of pitting corrosion on the passive film. The BM demonstrates a relatively higher breakdown voltages. Considering the passivation potential ranges and breakdown voltages for three conditions, it can be concluded that the BM shows relatively higher corrosion resistance, followed by DP-HEA, and lastly, SP-HEA.

Representative Nyquist plots for the BM, SP-HEA and DP-HEA in a 3.5% wt. NaCl electrolyte solution measured at their individual OCPs are shown in Fig. 7. It is clear the existence of capacitive loops in the low frequency regions, which possess the typical shape of passivation reactions [47,48]. Besides, as it is clear in the Nyquist diagrams, the order of the diameter of capacitive loops is a follow:  ${\rm BM} > {\rm SP-HEA} > {\rm DP-HEA}$ , which suggests that the BM has the highest corrosion resistance while SP-HEA has the lowest corrosion resistance [49,50]. This is consistent with the conclusions drawn from the polarization curves as discussed previously.

Based on the above discussion, comparison of the corrosion performance of SP-HEA and DP-HEA, this indicates that DP-HEA condition possesses a superior corrosion resistance, which can be attributed to its specific spatially-variable heterostructure, leading to better stability and durability in corrosive environments.

#### 4. Conclusions

This study successfully utilized pulse laser source for single- and double-side multi-pass processing to fabricate two distinct spatially heterogeneous structures (SP-HEA and DP-HEA) on an originally cold rolled CoCrFeMnNi HEA. The following main conclusions were drawn:

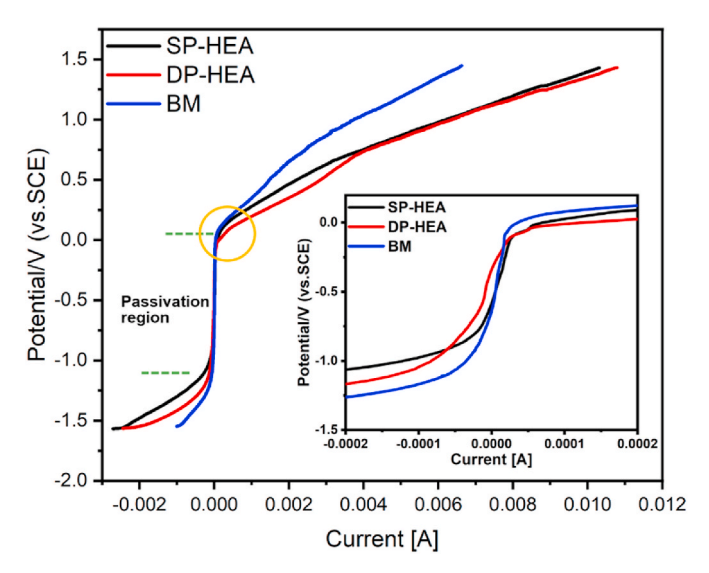
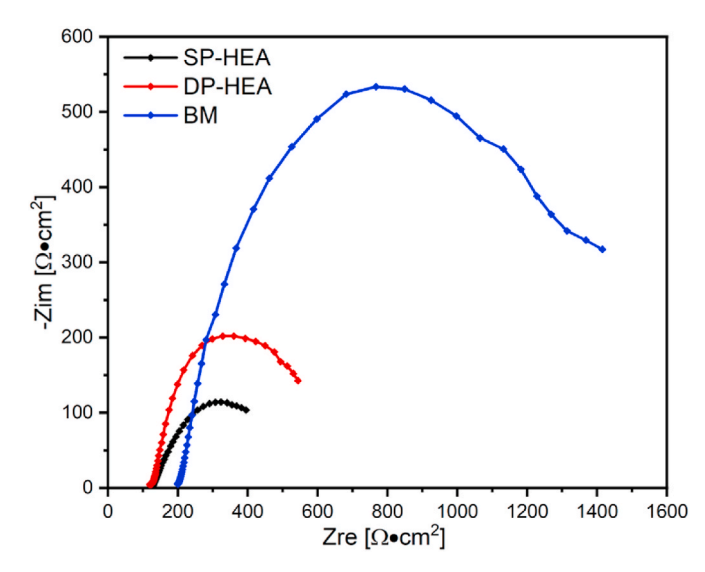


Fig. 6. Anodic polarization curve for BM, SP-HEA and DP-HEA.



**Fig. 7.** Nyquist impedance diagrams for the BM, SP-HEA and DP-HEA at open circuit potentials (OCP) in 3.5% wt. NaCl electrolyte solution.

- SP-HEA exhibited coarse columnar grains, while DP-HEA displayed a sandwich-like structure with fine equiaxed recrystallized grains.
- The significant differences in the microstructure distribution of these two spatially heterogeneous materials primarily stem from the distinctive thermal cycles imposed during processing.
- Tensile testing revealed that DP-HEA, double-side processed, exhibited higher ductility (≈18.9% vs. ≈ 11.0%) and ultimate strength (≈693 vs. ≈ 570 MPa) compared to SP-HEA. This is mainly due to the presence of large areas of high strength and ductility recrystallized heterogeneous microstructures, along with smaller strength disparities between the soft and hard domains in the material.
- The premature failure of SP-HEA at the soft-hard interface was caused by significant mechanical incompatibility, which promotes stress concentration and results in lower ductility and higher cracking susceptibility.
- DP-HEA exhibited enhanced corrosion resistance compared to SP-HEA, suggesting superior stability in corrosive environments.

These findings underscore the correlation between the distribution of spatially heterogeneous microstructures and mechanical properties. Through a detailed analysis of the distribution of spatially heterogeneous microstructures and their effect on the mechanical performance, this study offers valuable insights for material design and applications based on HEAs.

#### Originality statement

I write on behalf of myself and all co-authors to confirm that the results reported in the manuscript are original and neither the entire work, nor any of its parts have been previously published. The authors confirm that the article has not been submitted to peer review, nor has been accepted for publishing in another journal. The author(s) confirms that the research in their work is original, and that all the data given in the article are real and authentic. If necessary, the article can be recalled, and errors corrected.

#### CRediT authorship contribution statement

Jiajia Shen: Data curation, Formal analysis, Investigation, Writing – original draft. Yeon Taek Choi: Investigation. Jin Yang: Investigation. Jingjing He: Investigation. Zhi Zeng: Investigation. N. Zhou: Investigation. A.C. Baptista: Data curation, Formal analysis, Investigation.

**Hyoung Seop Kim:** Formal analysis, Investigation. **J.P. Oliveira:** Conceptualization, Data curation, Formal analysis, Supervision, Validation, Writing – review & editing.

#### Declaration of competing interest

The authors declare that they have no known competing financial interests or personal relationships that could have appeared to influence the work reported in this paper.

#### Data availability

Data will be made available on request.

#### Acknowledgments

JS and JPO acknowledge Fundação para a Ciência e a Tecnologia (FCT - MCTES) for its financial support via the project UID/00667/2020 (UNIDEMI). JS, ACB and JPO acknowledges the funding of CENIMAT/ i3N by national funds through the FCT-Fundação para a Ciência e a Tecnologia, I.P., within the scope of Multiannual Financing of R&D Units, reference LA/P/0037/2020, UIDP/50025/2020 and UIDB/ 50025/2020. JS acknowledges the China Scholarship Council for funding the Ph.D. grant (CSC NO. 201808320394). This work was supported by the National Research Foundation of Korea (NRF) grant funded by the Korea government (MSIP) (NRF-2022R1A5A1030054).

#### Appendix A. Supplementary data

Supplementary data to this article can be found online at https://doi.org/10.1016/j.msea.2024.146272.

#### References

- [1] G.H. Gu, R.E. Kim, J. Lee, H.S. Kim, Tailoring microstructure with spatial heterogeneity in CoCrFeMnNi high-entropy alloy via laser surface relaxation, Mater. Sci. Eng. 852 (2022) 143720, https://doi.org/10.1016/j. msea.2022.143720.
- [2] D. Li, C. Li, T. Feng, Y. Zhang, G. Sha, J.J. Lewandowski, P.K. Liaw, Y. Zhang, High-entropy Al0.3CoCrFeNi alloy fibers with high tensile strength and ductility at ambient and cryogenic temperatures, Acta Mater. 123 (2017) 285–294, https://doi.org/10.1016/j.actamat.2016.10.038.
- [3] N.K. Adomako, G. Shin, N. Park, K. Park, J.H. Kim, Laser dissimilar welding of CoCrFeMnNi-high entropy alloy and duplex stainless steel, J. Mater. Sci. Technol. 85 (2021) 95–105, https://doi.org/10.1016/j.jimst.2021.02.003.
- [4] G. Singh, H. Chan, A. Baskin, E. Gelman, N. Repnin, P. Král, R. Klajn, Self-assembly of magnetite nanocubes into helical superstructures, Science 84 345 (2014) 1149–1153, https://doi.org/10.1126/science.1254132.
- [5] Y.H. Jo, S. Jung, W.M. Choi, S.S. Sohn, H.S. Kim, B.J. Lee, N.J. Kim, S. Lee, Cryogenic strength improvement by utilizing room-temperature deformation twinning in a partially recrystallized VCrMnFeCoNi high-entropy alloy, Nat. Commun. 8 (2017) 15719, https://doi.org/10.1038/ncomms15719.
- [6] G.H. Gu, R.E. Kim, J. Lee, H.S. Kim, Tailoring microstructure with spatial heterogeneity in CoCrFeMnNi high-entropy alloy via laser surface relaxation, Mater. Sci. Eng. 852 (2022), https://doi.org/10.1016/j.msea.2022.143720.
- J.-W. Yeh, Alloy design strategies and future trends in high-entropy alloys,
   J. Occup. Med. 65 (2013) 1759–1771, https://doi.org/10.1007/s11837-013-0761-6.
- [8] Y. Han, H. Li, H. Feng, K. Li, Y. Tian, Z. Jiang, Enhancing the strength and ductility of CoCrFeMnNi high-entropy alloy by nitrogen addition, Mater. Sci. Eng. 789 (2020) 139587. https://doi.org/10.1016/j.msea.2020.139587.
- [9] X. Wu, Y. Zhu, Heterogeneous materials: a new class of materials with unprecedented mechanical properties, Mater. Res. Lett. 5 (2017) 527–532, https://doi.org/10.1080/21663831.2017.1343208.
- [10] Y. Wei, Y. Li, L. Zhu, Y. Liu, X. Lei, G. Wang, Y. Wu, Z. Mi, J. Liu, H. Wang, H. Gao, Evading the strength–ductility trade-off dilemma in steel through gradient hierarchical nanotwins, Nat. Commun. 5 (2014) 3580, https://doi.org/10.1038/ ncomms4580.
- [11] A.Y. Chen, L.L. Zhu, L.G. Sun, J.B. Liu, H.T. Wang, X.Y. Wang, J.H. Yang, J. Lu, Scale law of complex deformation transitions of nanotwins in stainless steel, Nat. Commun. 10 (2019), https://doi.org/10.1038/s41467-019-09360-1.
- [12] X.L. Wu, P. Jiang, L. Chen, J.F. Zhang, F.P. Yuan, Y.T. Zhu, Synergetic strengthening by gradient structure, Mater. Res. Lett. 2 (2014) 185–191, https://doi.org/10.1080/21663831.2014.935821.

- [13] A.Y. Chen, L.L. Zhu, L.G. Sun, J.B. Liu, H.T. Wang, X.Y. Wang, J.H. Yang, J. Lu, Scale law of complex deformation transitions of nanotwins in stainless steel, Nat. Commun. 10 (2019) 1403, https://doi.org/10.1038/s41467-019-09360-1.
- [14] X. Wu, M. Yang, F. Yuan, G. Wu, Y. Wei, X. Huang, Y. Zhu, Heterogeneous lamella structure unites ultrafine-grain strength with coarse-grain ductility, Proc. Natl. Acad. Sci. USA 112 (2015) 14501–14505, https://doi.org/10.1073/ pnas.1517193112.
- [15] Y. Wang, M. Chen, F. Zhou, E. Ma, High tensile ductility in a nanostructured metal, Nature 419 (2002) 912–915, https://doi.org/10.1038/nature01133.
- [16] Y. Zhao, T. Topping, J.F. Bingert, J.J. Thornton, A.M. Dangelewicz, Y. Li, W. Liu, Y. Zhu, Y. Zhou, E.J. Lavernia, High tensile ductility and strength in bulk nanostructured nickel, Adv. Mater. 20 (2008) 3028–3033, https://doi.org/10.1002/adma.200800214.
- [17] B.Q. Han, J.Y. Huang, Y.T. Zhu, E.J. Lavernia, Strain rate dependence of properties of cryomilled bimodal 5083 Al alloys, Acta Mater. 54 (2006) 3015–3024, https://doi.org/10.1016/j.actamat.2006.02.045.
- [18] C. Sawangrat, S. Kato, D. Orlov, K. Ameyama, Harmonic-structured copper: performance and proof of fabrication concept based on severe plastic deformation of powders, J. Mater. Sci. 49 (2014) 6579–6585, https://doi.org/10.1007/s10853-014-8258-4.
- [19] S.K. Vajpai, M. Ota, T. Watanabe, R. Maeda, T. Sekiguchi, T. Kusaka, K. Ameyama, The development of high performance Ti-6Al-4V alloy via a unique microstructural design with bimodal grain size distribution, Metall. Mater. Trans. 46 (2015) 903–914, https://doi.org/10.1007/s11661-014-2649-7.
- [20] Z. Zhang, S.K. Vajpai, D. Orlov, K. Ameyama, Improvement of mechanical properties in SUS304L steel through the control of bimodal microstructure characteristics, Mater. Sci. Eng. 598 (2014) 106–113, https://doi.org/10.1016/j. msea.2014.01.023.
- [21] P. Sathiyamoorthi, H.S. Kim, High-entropy alloys with heterogeneous microstructure: processing and mechanical properties, Prog. Mater. Sci. 123 (2022) 100709, https://doi.org/10.1016/j.pmatsci.2020.100709.
- [22] Y. Zhao, T. Topping, Y. Li, E.J. Lavernia, Strength and ductility of Bi-modal Cu, Adv. Eng. Mater. 13 (2011) 865–871, https://doi.org/10.1002/adem.201100019.
- [23] Y. Estrin, Y. Beygelzimer, R. Kulagin, P. Gumbsch, P. Fratzl, Y. Zhu, H. Hahn, Architecturing materials at mesoscale: some current trends, Mater. Res. Lett. 9 (2021) 399–421, https://doi.org/10.1080/21663831.2021.1961908.
- [24] H. Sun, F. Saba, G. Fan, Z. Tan, Z. Li, Micro/nano-reinforcements in bimodal-grained matrix: a heterostructure strategy for toughening particulate reinforced metal matrix composites, Scripta Mater. 217 (2022), https://doi.org/10.1016/j.scriptamat.2022.114774.
- [25] X. Wu, Y. Zhu, Gradient and lamellar heterostructures for superior mechanical properties, MRS Bull. 46 (2021) 244–249, https://doi.org/10.1557/s43577-021-00056-w.
- [26] H.H. Lee, J.I. Yoon, H.K. Park, H.S. Kim, Unique microstructure and simultaneous enhancements of strength and ductility in gradient-microstructured Cu sheet produced by single-roll angular-rolling, Acta Mater. 166 (2019) 638–649, https://doi.org/10.1016/j.actamat.2019.01.021.
- [27] J.G. Kim, J.H. Moon, A. Amanov, H.S. Kim, Strength and ductility enhancement in the gradient structured twinning-induced plasticity steel by ultrasonic nanocrystalline surface modification, Mater. Sci. Eng. 739 (2019) 105–108, https://doi.org/10.1016/j.msea.2018.10.045.
- [28] T.A. Listyawan, H. Lee, N. Park, U. Lee, Microstructure and mechanical properties of CoCrFeMnNi high entropy alloy with ultrasonic nanocrystal surface modification process, J. Mater. Sci. Technol. 57 (2020) 123–130, https://doi.org/ 10.1016/j.jmst.2020.02.083.
- [29] J.M. Park, E.S. Kim, H. Kwon, P. Sathiyamoorthi, K.T. Kim, J.H. Yu, H.S. Kim, Effect of heat treatment on microstructural heterogeneity and mechanical properties of 1%C-CoCrFeMnNi alloy fabricated by selective laser melting, Addit. Manuf. 47 (2021), https://doi.org/10.1016/j.addma.2021.102283.
- [30] P. Wang, J. Chen, B. Sun, D. Zhu, Y. Cao, Effects of annealing process parameters on microstructural evolution and strength-ductility combination of CoCrFeMnNi high-entropy alloy, Mater. Sci. Eng. 840 (2022) 142880, https://doi.org/10.1016/ i.msea.2022.142880.
- [31] C.X. Huang, Y.F. Wang, X.L. Ma, S. Yin, H.W. Höppel, M. Göken, X.L. Wu, H.J. Gao, Y.T. Zhu, Interface affected zone for optimal strength and ductility in heterogeneous laminate, Mater. Today 21 (2018) 713–719, https://doi.org/10.1016/j.mattod.2018.03.006.
- [32] G.M. Karthik, Y. Kim, E.S. Kim, A. Zargaran, P. Sathiyamoorthi, J.M. Park, S. G. Jeong, G.H. Gu, A. Amanov, T. Ungar, H.S. Kim, Gradient heterostructured laser-powder bed fusion processed CoCrFeMnNi high entropy alloy, Addit. Manuf. 59 (2022) 103131, https://doi.org/10.1016/j.addma.2022.103131.
- [33] G.H. Gu, E.S. Kim, H. Kwon, S. Son, R.E. Kim, T.G. Oh, H.S. Kim, Fabrication of multi-gradient heterostructured CoCrFeMnNi high-entropy alloy using laser metal deposition, Mater. Sci. Eng. 836 (2022) 142718, https://doi.org/10.1016/j. msea.2022.142718.
- [34] R.E. Kim, G.M. Karthik, A. Amanov, Y.-U. Heo, S.G. Jeong, G.H. Gu, H. Park, E. S. Kim, D.W. Lee, H.S. Kim, Superior gradient heterostructured alloys fabricated by laser powder bed fusion via annealing and ultrasonic nanocrystal surface modification, Scripta Mater. 230 (2023) 115422, https://doi.org/10.1016/j.scriptamat.2023.115422.
- [35] G.M. Karthik, Y. Kim, E.S. Kim, A. Zargaran, P. Sathiyamoorthi, J.M. Park, S. G. Jeong, G.H. Gu, A. Amanov, T. Ungar, H.S. Kim, Gradient heterostructured laser-powder bed fusion processed CoCrFeMnNi high entropy alloy, Addit. Manuf. 59 (2022), https://doi.org/10.1016/j.addma.2022.103131.
- [36] C. Nagarjuna, J.W. Song, K.Y. Jeong, M.W. Pin, G. Song, J.K. Lee, Y.S. Na, H. S. Kim, K.B. Kim, S.J. Hong, Developing harmonic structure in CoCrFeMnNi high

- entropy alloy to enhance mechanical properties via powder metallurgy approach, J. Mater. Res. Technol. 17 (2022) 1686–1695, https://doi.org/10.1016/j.imrt.2022.01.098.
- [37] J.P. Oliveira, J. Shen, Z. Zeng, J.M. Park, Y.T. Choi, N. Schell, E. Maawad, N. Zhou, H.S. Kim, Dissimilar laser welding of a CoCrFeMnNi high entropy alloy to 316 stainless steel, Scripta Mater. 206 (2022) 114219, https://doi.org/10.1016/j. scriptamat.2021.114219.
- [38] Y.F. Wang, M.S. Wang, X.T. Fang, F.J. Guo, H.Q. Liu, R.O. Scattergood, C.X. Huang, Y.T. Zhu, Extra strengthening in a coarse/ultrafine grained laminate: role of gradient interfaces, Int. J. Plast. 123 (2019) 196–207, https://doi.org/10.1016/j.iiplas.2019.07.019
- [39] Y. Kim, G.H. Gu, H.S. Kim, Fundamental analysis of deformation behavior in coreshell heterostructured materials, Comput. Mater. Sci. 215 (2022) 111818, https:// doi.org/10.1016/j.commatsci.2022.111818.
- [40] Y. Zhu, X. Wu, Perspective on hetero-deformation induced (HDI) hardening and back stress, Mater. Res. Lett. 7 (2019) 393–398, https://doi.org/10.1080/ 21663831.2019.1616331.
- [41] R.E. Kim, E.S. Kim, G.M. Karthik, G.H. Gu, S.Y. Ahn, H. Park, J. Moon, H.S. Kim, Heterostructured alloys with enhanced strength-ductility synergy through lasercladding, Scripta Mater. 215 (2022) 114732, https://doi.org/10.1016/j. scriptamat.2022.114732.
- [42] G.H. Gu, R.E. Kim, J. Lee, H.S. Kim, Tailoring microstructure with spatial heterogeneity in CoCrFeMnNi high-entropy alloy via laser surface relaxation, Mater. Sci. Eng. 852 (2022) 143720, https://doi.org/10.1016/j. msez.2022143720
- [43] G.M. Karthik, Y. Kim, E.S. Kim, A. Zargaran, P. Sathiyamoorthi, J.M. Park, S. G. Jeong, G.H. Gu, A. Amanov, T. Ungar, H.S. Kim, Gradient heterostructured laser-powder bed fusion processed CoCrFeMnNi high entropy alloy, Addit. Manuf. 59 (2022) 103131, https://doi.org/10.1016/j.addma.2022.103131.

- [44] S.J. Sun, Y.Z. Tian, H.R. Lin, X.G. Dong, Y.H. Wang, Z.J. Zhang, Z.F. Zhang, Enhanced strength and ductility of bulk CoCrFeMnNi high entropy alloy having fully recrystallized ultrafine-grained structure, Mater. Des. 133 (2017) 122–127, https://doi.org/10.1016/j.matdes.2017.07.054.
- [45] H.R. Lin, Y.Z. Tian, S.J. Sun, Z.J. Zhang, Y. Bai, J.T. Lu, Z.F. Zhang, N. Tsuji, Significant transitions of mechanical properties by changing temperature in Cu-Al alloys with heterogeneous microstructures, Mater. Char. 168 (2020) 110546, https://doi.org/10.1016/j.matchar.2020.110546.
- [46] C.W. Shao, P. Zhang, Y.K. Zhu, Z.J. Zhang, Y.Z. Tian, Z.F. Zhang, Simultaneous improvement of strength and plasticity: additional work-hardening from gradient microstructure, Acta Mater. 145 (2018) 413–428, https://doi.org/10.1016/j. actamat.2017.12.028.
- [47] B. Messaoudi, S. Joiret, M. Keddam, H. Takenouti, Anodic behaviour of manganese in alkaline medium, Electrochim. Acta 46 (2001) 2487–2498, https://doi.org/ 10.1016/S0013-4686(01)00449-2.
- [48] J. Yang, J. Wu, C.Y. Zhang, S.D. Zhang, B.J. Yang, W. Emori, J.Q. Wang, Effects of Mn on the electrochemical corrosion and passivation behavior of CoFeNiMnCr high-entropy alloy system in H2SO4 solution, J. Alloys Compd. 819 (2020) 152943, https://doi.org/10.1016/j.jallcom.2019.152943.
- [49] M. Izadi, M. Soltanieh, S. Alamolhoda, S.M.S. Aghamiri, M. Mehdizade, Microstructural characterization and corrosion behavior of AlxCoCrFeNi high entropy alloys, Mater. Chem. Phys. 273 (2021) 124937, https://doi.org/10.1016/j. matchemphys.2021.124937.
- [50] M. Mehdizade, A.R. Eivani, M. Soltanieh, Effects of reduced surface grain structure and improved particle distribution on pitting corrosion of AA6063 aluminum alloy, J. Alloys Compd. 838 (2020) 155464, https://doi.org/10.1016/j. iallcom.2020.155464.